RESEARCH ARTICLE

Check for updates

Electrochemically triggered rational design of bismuth copper sulfide for wearable all-sulfide semi-solid-state supercapacitor with a wide operational potential window (1.8 V) and ultra-long life†

Edugulla Girija Shankar, Bhimanaboina Ramulu, [ID] Manchi Nagaraju and Jae Su Yu [ID] *

There has been a growing need for supercapacitors (SCs) as a promising energy storage device with high energy and power densities. For this reason, electrodes with a wide operational potential window (OPW) and high capacity are desirable for energy storage. Previously, carbon-based electrodes were mostly used as a negative electrode in SCs, but their low capacity and narrow OPW hindered the performance of the SCs. Hence, a novel binder-free faradaic type bismuth copper sulfide (BCS) electrode has been synthesized in 600 s at room temperature *via* a simple and swift electrodeposition (ED) method. The effect of the Bi and Cu molar concentrations in the growth solution ($Bi_xCu_{3-x}S_3$) on its crystal structure and surface morphology is investigated during the ED process to further understand the synergistic benefits of Bi and Cu ions for enhanced electrochemical performance. The optimized BCS electrode exhibits excellent electrochemical properties with a wide OPW of 1.2 V and a specific capacity of 290 mA h g^{-1}. Additionally, nickel sulfide (NS) as a faradaic type positive electrode is synthesized *via* the ED. The BCS and NS electrodes are employed as negative and positive electrodes, respectively, to fabricate a novel gel electrolyte-based wearable all-sulfide semi-solid-state SC (ASSSC). The ASSSC device maintains ~100% capacitance retention across the 40 000 charge−discharge cycles. Furthermore, two serially connected ASSSC devices are attached to the human fingers to power the electronic gadgets using various finger movements.

1. Introduction

Demand for economical, highly efficient, flexible, lightweight, and wearable energy storage devices is increasing in day-to-day life. Supercapacitors (SCs) have attracted much attention due to their advantages such as rapid charge−discharge rates, low cost, eco-friendliness feature, safe operation, and long life.[1] For modern wearable electronics, carbon cloth (CC) is being extensively used as a current collector for flexible SCs because of its high electrical conductivity, flexibility, and mechanical toughness.[2] However, despite their merits, the SCs suffer from incompetent energy density when compared to batteries, limiting their real-life application as an efficient energy storage device.[3] The energy density (E) can be calculated using $E = 0.5 \times CV^2$, where C and V represent the capacitance and operational potential window (OPW), respectively. Considering the following, the SCs comprised of electrodes with a wide OPW and high capacitance can enhance the energy density. This evolved into the concept of asymmetric SCs (ASCs) consisting of different electrodes with high electroactive sites, wide OPW, and fast ion-electron transfer kinetics. So far, various metal oxide and chalcogen-based positive electrode materials for SCs have been reported with satisfactory results.[4] Graphene-based materials as well as typical carbonaceous materials such as activated carbon and biomass-derived carbon have been reported.[5] However, a limited specific capacitance (C_s) and OPW fails to enhance the energy density of the ASC, impeding its commercialization. Therefore, a negative electrode with a wide OPW and high C_s is extremely desirable to assemble an ASC with enhanced energy density.

*Department of Electronics and Information Convergence Engineering, Institute for Wearable Convergence Electronics, Kyung Hee University, 1732 Deogyeong-daero, Giheung-gu, Yongin-si, Gyeonggi-do 17104, Republic of Korea.
E-mail: jsyu@khu.ac.kr*

3270 | *Inorg. Chem. Front.*, 2024, **11**, 3270–3284

This journal is © the Partner Organisations 2024

In this respect, electrode materials with a multielectron transfer can offer a promising way to enhance the capacitance in an aqueous alkaline medium.[6,7] Bismuth (Bi)-based electrode materials show multiple reversible redox reactions in an aqueous alkaline medium, unveiling a distinct "quasi-conversion reaction" mechanism ($Bi_2O_3 \Leftrightarrow Bi^0$).[8] According to previous studies, Bi_2O_3 exhibits a very high specific capacity (C_{ts}) of 345.11 mA h g^{-1}. Recently, copper-based materials have been employed as a negative electrode due to their unique property and high theoretical capacity in an alkaline medium with a wide OPW below 0 V (vs. H/H^+).[9,10] Furthermore, the addition of sulfur (S) to the crystal structure of a bimetallic structure is anticipated to boost the electrochemical properties due to the lower electronegativity and higher electrical conductivity ($S = 5 \times 10^{-28}$ S m^{-1}) of S when compared to O.[11,12] Inspired by the following, in this work, novel bismuth copper sulfide (BCS) was synthesized and employed as a negative electrode in the SC device.

Recently, nickel sulfide (NS) electrode materials have been intensively studied for use as a positive electrode in an SC device. The Heazlewoodite structure of NS consists of four Ni–Ni bonds, and the following bonds are shorter compared to the Ni–Ni bond in the Ni metal, further leading to the demonstration of enhanced electrochemical properties and electrical conductivity when compared to the other Ni-based compounds.[13] The NS has been used as a positive electrode in the SC device. Generally, metal chalcogenide (Bi_2S_3, Ni_2S_3, CoS_2, and so on) electrode materials have been synthesized using complicated hydrothermal and solvothermal methods.[14] However, the following synthesis method involves long synthesis time, high temperature, low mass loading, and no growth control. In this respect, the electrodeposition (ED) method has emerged as a promising and simple binder-free synthesis technique to synthesize metal chalcogenides under room temperature conditions. The advantages of the ED method, such as single-step synthesis, growth control, short duration, and room temperature synthesis, make it a potential technique for bulk synthesis.[15] In addition, binder-free methodology further enhances the electron transport and electroactive sites.

Encouraged by the following, the present work demonstrated the synthesis and fabrication of the novel BCS/CC and NS/CC as negative and positive electrodes, respectively via a simple ED method to produce wearable all-sulfide semi-solid-state SC (ASSSC). The effect of the Bi : Cu molar concentration ratio in the $Bi_xCu_{3-x}S_3$ growth solution on the crystal structure, the surface morphology, and electrochemical properties was investigated. An interconnected three-dimensional (3D) network of nanosheet arrays was obtained for $Bi_1Cu_2S_3$ ($x = 1$), further benefiting the electrolyte interaction with the electroactive site. Moreover, uniformly distributed arrays of nanoparticle morphology were obtained for NS, and their electrochemical properties were studied. Furthermore, a novel ASSSC device was fabricated by employing optimized BCS and NS electrodes as negative and positive electrodes, respectively, using a poly(vinyl alcohol) (PVA)–KOH gel-based semi-solid-state electrolyte. The structural and mechanical well-integrated free-standing electrode materials on CC (the ASSSC device) demonstrated an ultra-long life with an excellent cycling stability performance. Also, a wearable ASSSC device attached to human fingers was employed as a power source to power a digital display and an electric motor under various finger movements, demonstrating a real-life practical application. The following results suggest the potential application of the ASSSC device for next-generation advanced energy storage applications.

2. Experimental section

2.1. Preparation of a $Bi_xCu_{3-x}S_3$/CC negative electrode and a NS positive electrode

Initially, an efficient amount of the CC substrate (2 × 1 pieces) was functionalized with oxygen by treating it with concentrated HNO_3 at 70 °C for 6 h and it was further cleaned with deionized water (DIW) and ethanol to remove impurities, followed by drying at 70 °C for 6 h. The following enhances the hydrophilicity of the CC substrate, which anchors the uniform growth of the electrode material by enhancing nucleation sites and the surface activity of the CC substrate, which results in an improved electrode–electrolyte interaction by facilitating rapid absorption and desorption, helping to boost the electrochemical properties. The CC exposing the 1 × 1 cm^2 area was attached to the poly(ethylene terephthalate) (PET) sheet to prevent the backside coating. To synthesize the $BiCu_2S_3$ on the CC, bismuth(III) nitrate pentahydrate (1 mmol), copper nitrate trihydrate (2 mmol), sodium sulfate anhydrous (3 mmol), and lithium chloride (8 mmol) were dissolved in 40 ml of DIW and the pH of the growth solution was adjusted to ~3 using concentrated hydrochloric acid. In addition, the growth solution was bubbled with nitrogen gas to remove the dissolved oxygen. A conventional three-electrode setup was used for the ED, where CC, Ag/AgCl, and platinum (Pt) wire served as the working, reference, and counter electrodes, respectively. The $BiCu_2S_3$ nanosheet arrays on the CC were grown at a constant voltage of −1 V for 600 s using a chronoamperometry method. The fabricated electrode was flushed with DIW and ethanol to remove the unreacted elements and dried at 70 °C for 6 h. The following electrode was denoted as BCS-x ($x = 1$, where 'x' denotes the mmol concentration of Bi in the growth solution). To further analyze the effect of the Bi : Cu molar concentration ratio in the growth solution on the crystal structure and electrochemical properties, additional two electrodes were synthesized by varying the 'x' value to 0.5 and 2 under the same conditions. The electrodes obtained were denoted as BCS-0.5 and BCS-2. An almost similar electrode material mass was acquired by all three electrodes (~3 mg cm^{-2}). Furthermore, a similar ED technique was employed to prepare the NS electrode as a positive electrode by changing the growth solution. For the growth solution, 2 mmol nickel sulfate hexahydrate, 3 mmol sodium sulfate anhydrous, and 8 mmol lithium

This journal is © the Partner Organisations 2024

Inorg. Chem. Front., 2024, **11**, 3270–3284 | **3271**

chloride were dissolved in 40 ml of DIW and the ED parameters and conditions were kept similar to those of the negative electrode. The obtained electrode was denoted as NS.

2.2. Electrochemical properties

Cyclic voltammetry (CV), galvanostatic charge–discharge (GCD), and electrochemical impedance spectroscopy (EIS) (frequency range from 100 kHz to 0.01 Hz) measurements were performed individually for all the as-prepared electrodes to study the electrochemical properties in a three-electrode system. Here, Pt wire, Ag/AgCl, and the as-prepared electrodes served as counter, reference, and working electrodes, respectively. Fig. 1 shows a schematic illustration for the synthesis of the BCS-1 and NS electrodes.

2.3. Assembly of wearable ASSSC device

Prior to assembly, the PVA-KOH gel-based semi-solid-state electrolyte was prepared as reported in a previous report.[16] A wearable ASSSC device based on two electrodes was assembled as shown in Fig. 1, with the BCS-1 and NS as the

negative and positive electrodes, respectively. Whatman 42 filter paper (used as the separator) was soaked in a semi-solid-state electrolyte and then sandwiched between the negative and positive electrodes. After the solid-state electrolyte was semi-solidified, parafilm tape was employed to seal the assembly. The shape adaptability of the semi-solid-state electrolyte fits well with the wearable ASSSC device, thus avoiding the leakage problem of using liquid electrolytes and dissolution/pealing out during electrochemical analysis. To maximize the electrochemical performance of the ASSSC device, a well-known charge balance equation was employed to obtain the optimized mass ratios of the negative and positive electrodes:[17]

$$\frac{m_+}{m_-} = \frac{C_{m-}}{C_{m+}} \tag{1}$$

where $C_{m,\ Cm+}$ and m specify the capacity and mass, respectively, for the negative (−) and positive (+) electrodes as achieved in the three-electrode setup. The formulae used for C_{ts}, C_s, E, and power density are shown in the ESI.†
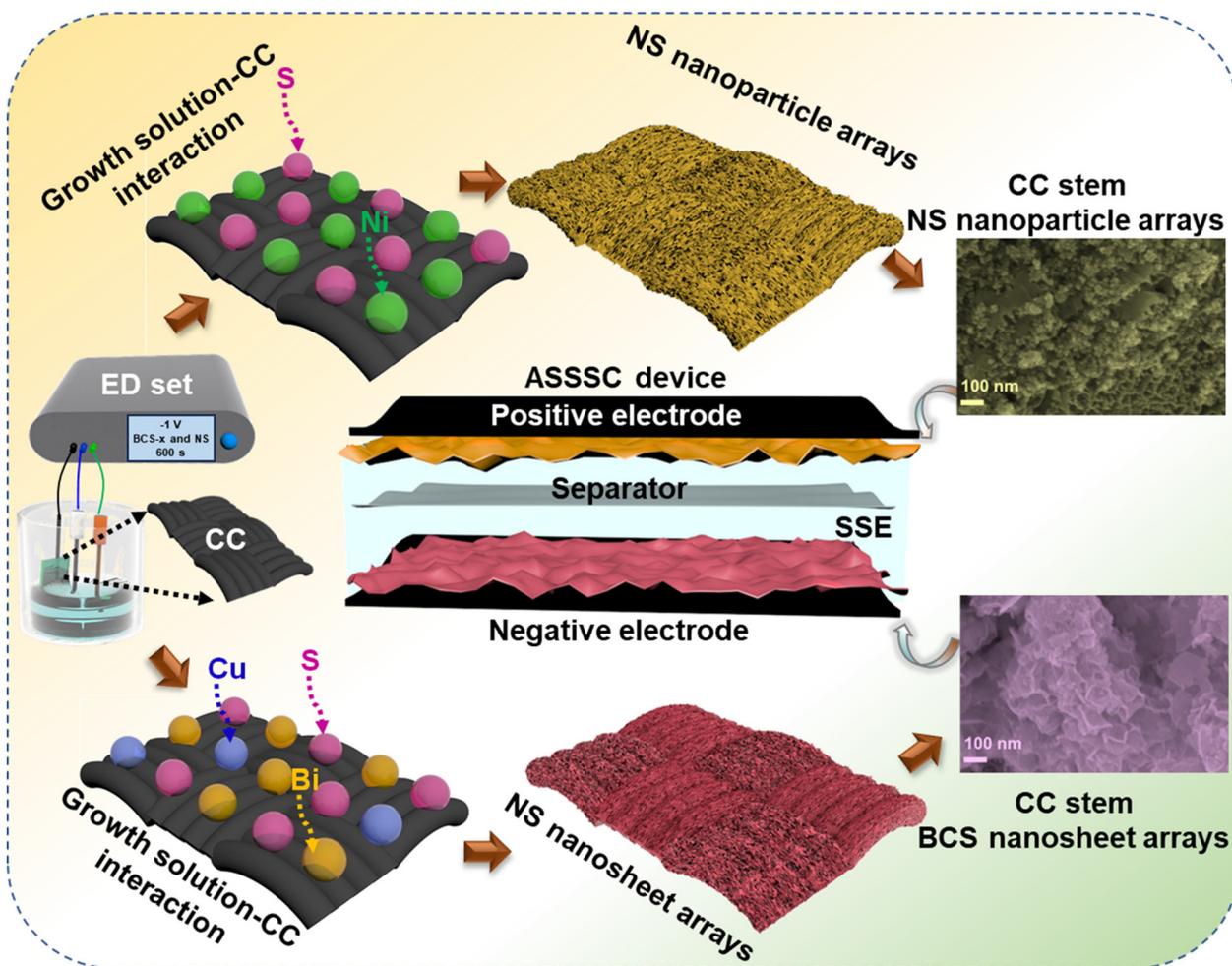

Fig. 1 A schematic representation displaying the simple synthesis of BCS-*x* and NS on a flexible CC current collector and assembly of the ASSSC device.

3272 | *Inorg. Chem. Front.*, 2024, **11**, 3270–3284

This journal is © the Partner Organisations 2024

3.   Results and discussion

The present work was designed to fabricate an entirely electro-chemically triggered all-sulfide SC as a facile and low-cost advanced wearable energy storage device. The overall C_s of the ASSSC device is wholly dependent on the individual C_s of the negative and positive electrodes, according to the following relationship:[18]

$$\frac{1}{C_t} = \frac{1}{C_p} + \frac{1}{C_n} \tag{2}$$

where C_t, C_p, and C_n indicate the total C_s of the ASSSC device, and the individual C_s of BCS-1 and NS electrodes, respectively. Here, the faradaic type BCS-1 electrode was employed as a negative electrode with the aim to broaden the OPW and increase the C_s of the ASSSC device, whereas the NS electrode was employed as a positive electrode to enhance the faradaic properties of the ASSSC device. Furthermore, the as-prepared electrodes were used for characterization and electrochemical performances.

To study the surface morphology of the as-prepared BCS-x and NS electrodes, field-emission scanning electron micro-scope (FE-SEM) analysis was employed as shown in Fig. 2. The effect on the surface morphology with different molar concentration ratios of Bi : Cu in growth solution was studied using the FE-SEM images. The surface morphology of BCS-0.5 is shown in Fig. 2(a) (i and ii). The FE-SEM images revealed the mixed morphology of nanosheets infused with coagulated nanoparticle arrays. The FE-SEM images of the BCS-1 showed the uniform growth of the densely packed vertically aligned nanosheet arrays on CC, as shown in Fig. 2(b) (i and ii). This result suggests that the woven CC fiber acted as an excellent scaffold for uniform growth of the nanosheet arrays with strong adhesion of electrode material and CC, making it a robust electrode, which may further support the long stability of the electrochemical cycles. The high magnification image showed that the average thickness of the nanosheets is ∼35 nm and they are interconnected with each other, creating a 3D porous structure. This may benefit the accessibility of the electroactive sites for the electrolyte during the electrochemical process. The FE-SEM images (Fig. 2(c) (i and ii)) of BCS-2 revealed an increase in the thickness and non-uniformity of the sheets upon increasing the Bi molar concentration in the growth solution. The FE-SEM images verified that the BiCu$_2$S$_3$ was the optimized growth solution to obtain the uniform and strongly adhered nanosheet arrays with CC fiber. Next, the uniformly distributed nanoparticles with an uneven size are adhesively supported on CC fiber as shown by the FE-SEM images of NS in Fig. 2(d) (i and ii). The interconnected nanoparticles further act as a bridge for electronic transmission, which significantly benefits the charge transfer process. Furthermore, the strongly adhered integrated EM-CC fiber can provide enhanced conductivity and short reaction path during the redox reaction of the EC process. Additionally, energy-dispersive X-ray spectroscopy (EDS) was performed to determine the elemental presence and distribution in BCS-1 and NS. Fig. 2(e and g) show the presence of Bi, Cu and S in the BCS-1 electrode and Ni and S in the NS electrode. Furthermore, elemental analysis suggests the uniform distribution of the detected elements in both BCS-1 and NS electrodes, as shown in Fig. 2(f) (i–iv) and (h) (i, ii). In addition, transmission electron microscope (TEM) and high-resolution (HR)-TEM were employed to study the internal structure of the BCS-x samples, as shown in Fig. S1 of the ESI.† The obtained results were in good agreement with those of the FE-SEM results. From Fig. S1(a and b) of the ESI,† the BCS-0.5 sample confirmed the presence of both clusters of nanoparticles and nanosheets in an infused form. For the BCS-1 sample, the presence of interconnected nanosheets with decent transparency suggests a thin 2D morphology, as shown in Fig. S1(d and e) of the ESI.† From Fig. S1(g and h) of the ESI,† a decrease in the sheet length with a low transparency was observed in the BCS-2 sample, suggesting an increase in the sheet thickness. Moreover, the HR-TEM analysis was performed for all the BCS-x samples together with the selected area electron diffraction (SAED) pattern. From the HR-TEM results (Fig. S1(c, f and i) of the ESI†), all the BCS-x samples demonstrated that the lattice fringes were aligned in various orientations with the SAED pattern containing the bright rings, which indicated the polycrystalline nature. The insets of the HR-TEM images showed the corresponding SAED pattern of each BCS-x sample.

The X-ray diffraction (XRD) technique was employed to investigate the crystal structure and phase of all the negative electrodes with different molar concentration ratios of Bi : Cu in growth solution (BCS-x), together with the positive (NS) electrode, as shown in Fig. 3(a and b). From the results, the BCS-1 and BCS-2 materials exhibited similar diffraction patterns with the characteristic diffraction peaks of orthorhombic BiCuS$_2$. The diffraction peaks at 27.19°, 29.02°, 30.98°, 33.26°, 37.98°, 39.72°, 47.70°, 48.83°, 50.17°, 51.19°, 62.19°, and 64.56° are indexed as (111), (031), (220), (131), (060), (160), (170), (251), (251), (340), (162), and (100), respectively according to the JCPDS card no. 00-002-0516 (Fig. 3(a)). Furthermore, lattice parameters (a, c), full width at half maximum (FWHM), volume (V), and crystallite size (D) of the BCS-1 and BCS-2 were calculated using the diffraction peak at 37.98° to investigate the effect of the molar concentration ratio of Bi : Cu in growth solution on the crystal structure using the well-known relationship:[19]

$$a = \lambda/\sqrt{3} \sin\theta; \ c = \lambda/\sin\theta; \ D = k\lambda/\beta_{hkl}\cos\theta; \ V = 0.85(a^2c) \tag{3}$$

The comparative values are shown in Table 1. A comparative variation of all the values was observed among the BCS-1 and BCS-2. This result implied that a change in the molar concentration ratio of Bi : Cu in the growth solution affected the crystal structure. However, for BCS-0.5, the characteristic diffraction peaks of BiCuS$_2$ were not matched. It is evident that a minimum of 1 mmol and 2 mmol of Bi and Cu, respectively, should be present in the growth solution to form the BiCuS$_2$
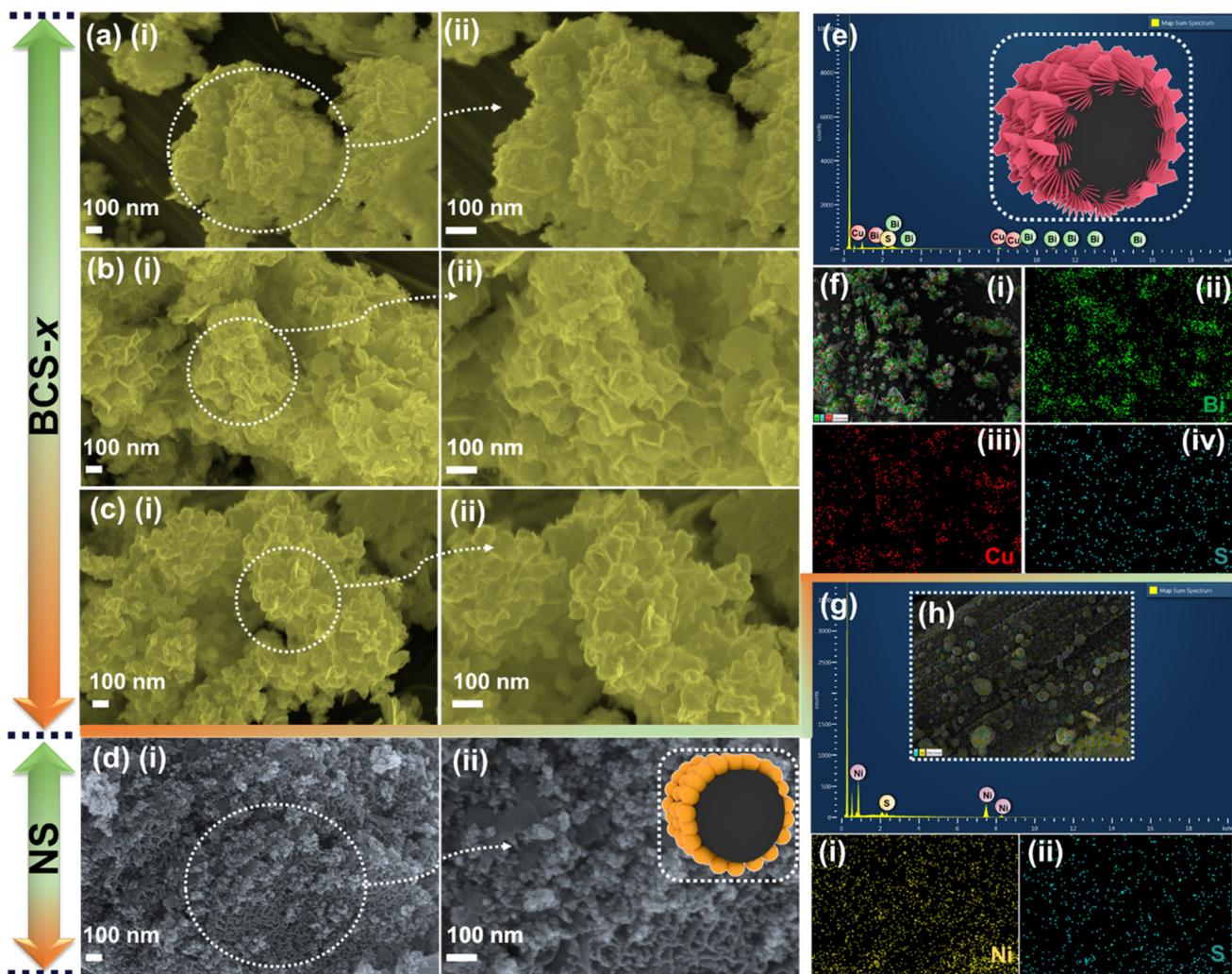
This journal is © the Partner Organisations 2024

Inorg. Chem. Front., 2024, **11**, 3270–3284 | **3273**

Fig. 2 FE-SEM images of the (a) BCS-0.5, (b) BCS-1, (c) BCS-2, and (d) NS materials at different magnifications. (e) and (g) EDS spectra and (f) (i)–(iv) and (h) (i), (ii) elemental mapping images of the BCS-1 and NS materials, respectively.

phase. Additionally, the NS exhibited the peaks at 29.10°, 31.06°, 33.37°, 40.50°, and 47.83°, which is matched with the rhombohedral NS and indexed as (101), (222), (300), (211), and (131), respectively, according to the JCPDS card no. 00-002-1443. Furthermore, the lattice parameters (a, c), FWHM, V, and D were calculated using a peak at 31.06° for NS and this is shown in Table 1. Fig. 3(b) shows the crystal structure retrieved from the vista software, where each Cu^{1+} atom is connected to four S^{2-} atoms, forming CuS_4 tetrahedra corners connected with eight equivalent BiS_5 square pyramids and corners connected with four equivalent CuS_4 tetrahedra.

The X-ray photoelectron spectroscopy (XPS) analysis was performed to investigate the surface elemental composition of the BCS-1 and NS electrodes. The full survey scan spectrum of the BCS-1 is shown in Fig. 3(c), confirming the presence of Bi, Cu, and S elements. The high-resolution (HR)-XPS spectrum of the Bi 4f is shown in Fig. 3(d). The spectrum consists of dual contributions due to the presence of various valences. The

results suggest the presence of the trivalent and pentavalent Bi in BCS-1. The peaks at 158.75 and 164.52 eV correspond to Bi^{3+} and the peaks at 159.25 and 164.04 eV are related to Bi^{5+}.[20] The HR-XPS spectrum of Cu 2p is illustrated in Fig. 3(e). The strong peak at 934.01 eV corresponds to Cu $2p_{3/2}$, whereas the peaks at 953.99 and 932.33 eV correspond to the Cu $2p_{1/2}$ which confirms the presence of metallic copper in two different states (+1, +2) and successively verifies the successful reduction of copper nitrate trihydrate by the applied voltage during the ED process.[21] Furthermore, ∼20 eV difference was observed between the peaks of Cu $2p_{1/2}$ and Cu $2p_{3/2}$, which shows the presence of Cu^{2+} in the BCS-1 electrode.[22] Two strong satellite peaks (denoted as sat.) were observed at 962.34 and 943.57 eV, which is attributed to the paramagnetic chemical state of Cu^{2+}.[22] In addition, the typical characteristic peak of copper oxide was observed at 940.4 eV, indicating the uniform oxidation of the copper crystals upon exposure to the atmosphere.[23] The HR-XPS spectrum of S 2p (Fig. 3(f)) shows
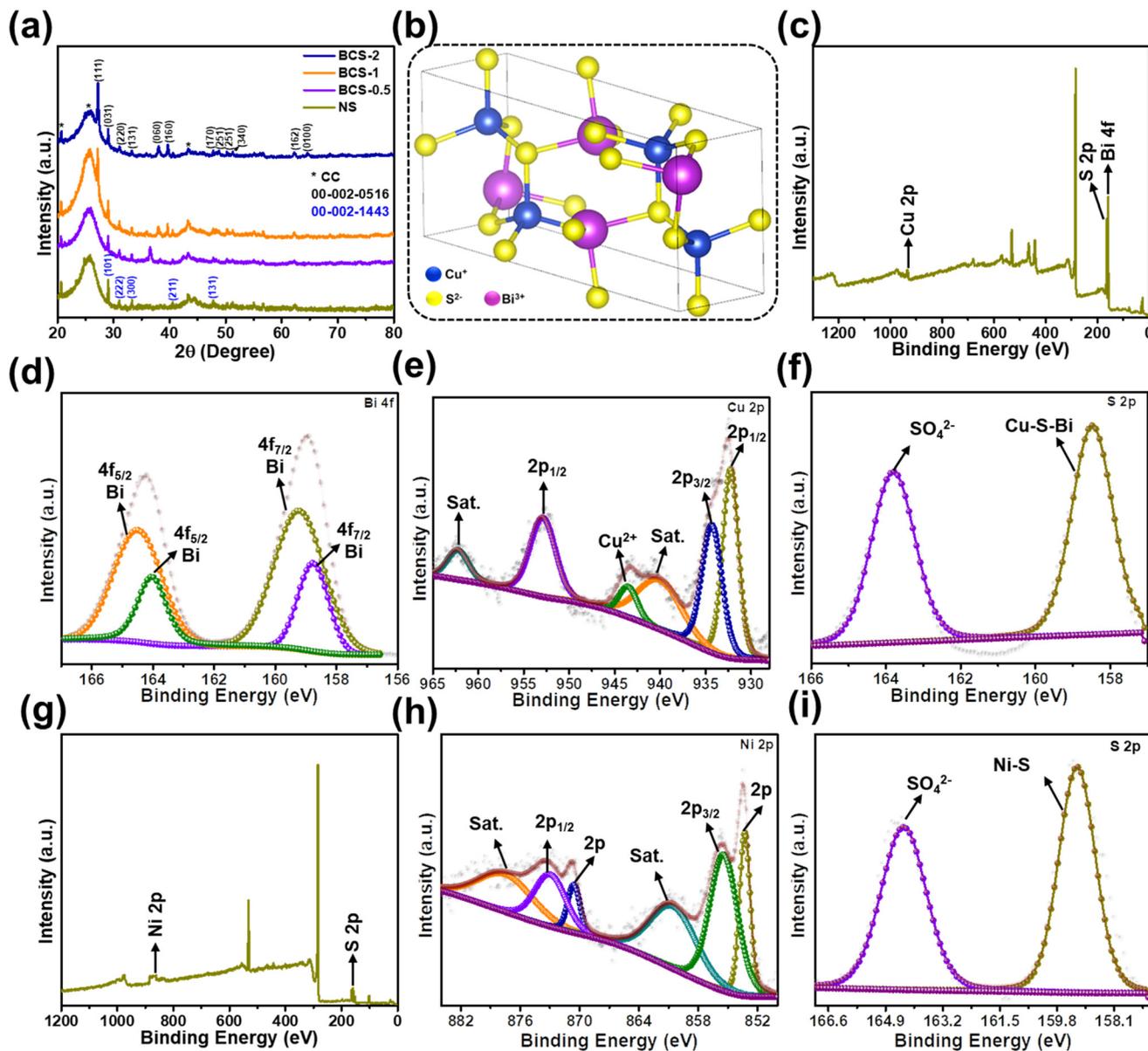
Fig. 3 (a) XRD patterns of all the prepared electrodes and (b) schematic illustration of the crystal structure of BCS-1. (c) XPS survey scan spectrum of the BCS-1 material and HR-XPS spectra of (d) Bi 4f, (e) Cu 2p, and (f) S 2p. (g) XPS survey scan spectrum of the NS material and HR-XPS spectra of (h) Ni 2p and (i) S 2p.

Table 1 Comparison of the lattice parameters, FWHM, d spacing, and crystallite size of the prepared electrode materials

Sample name	a (Å)	c (Å)	FWHM (degree)	V (Å^3)	D (nm)
BCS-1	2.73	4.73	0.41	0.272	21.27
BCS-2	2.72	4.72	0.45	0.271	19.41
NS	3.32	5.75	0.73	0.267	11.76

two strong peaks at 158.46 and 163.8 eV which correspond to the SO_4^{2-} ions and the Bi–S–Cu, respectively. The presence of the Bi–S–Cu peak confirms the bonding of the S with both the Cu^+ and Bi^+ sites. Moreover, the FWHM value of the Bi–S–Cu

peak was observed to be greater than that of the SO_4^{2-} ions, which may benefit the electrochemical properties due to the synergistic effect.[21] Next, the XPS was also performed for the NS electrode to study the elemental composition and oxidation. The survey scan spectrum confirmed the presence of the Ni and S elements as shown in Fig. 3(g). The HR-XPS spectrum of Ni 2p is shown in Fig. 3(h), and the peaks at 855.62 and 873.12 eV correspond to Ni $2p_{3/2}$ and $2p_{1/2}$, respectively, together with the satellite peaks at 877.61 and 860.65 eV, which suggested the presence of the Ni species as Ni^{2+} and Ni^{3+}. In addition, two peaks at 870.71 and 853.35 eV were observed, corresponding to zero valent metallic Ni.[24,25] The HR-XPS spectrum of the S 2p of the NS electrode was similar

This journal is © the Partner Organisations 2024

Inorg. Chem. Front., 2024, **11**, 3270–3284 | **3275**

to that of the BCS-1 electrode, as shown in Fig. 3(i). The two strong peaks at 159.20 and 164.3 eV correspond to the SO_4^{2-} ions and Ni–S, respectively. The Ni–S peak confirmed the bonding of the S with the Ni^+ sites. Furthermore, the greater FWHM value of the Ni–S peak compared to the SO_4^{2-} ion peak may further benefit the electrochemical properties due to the synergistic effect.[21]

To further determine the elemental ratio of the as-prepared BCS-1 and NS samples, inductively coupled plasma (ICP) spectroscopy was performed. It is worth noting that the detection of the sulfur content in the sample was not possible using the ICP technique because sulfur has a high ionization potential, reducing the sensitivity and further intense polyatomic interferences affect all the isotopes of sulfur. In this respect, the atomic ratio percentages of Bi and Cu were found to be 19.7% and 80.2%, respectively, for the BCS-1 sample, and the Ni content in the NS sample was also determined, as shown in Fig. S2(a and b) in the ESI.† The ICP spectroscopy confirmed the presence of the Bi and Cu contents in the BCS-1 sample, whereas the Ni content in the NS sample also agreed well with the EDS and XPS results.

The electrochemical properties of all the as-prepared BCS-x were evaluated as discussed in the Experimental section. Initially, comparative CV analysis was performed with a fixed scan rate of 10 mV s^{-1} and the OPW of 0 to −1.2 V in the three-electrode cell is illustrated in Fig. 4(a). From these results, it was seen that the BCS-x electrodes demonstrated a similar redox CV nature. It was evident that the redox peaks were predominantly generated by the reaction of BiCuS$_2$ (BiCuS$_2$ + OH$^-$ ⇌ BiCuS$_2$OH + H$_2$O + e$^-$), indicating the dominant faradaic type charge storage behavior.[26] However, a change in the integral area of the CV curves was observed in the BCS-x samples, verifying the effect of the molar concentration ratio of Bi : Cu in the growth solution. Among the BCS-x electrodes, the BCS-1 electrode demonstrated the superior area under the CV curve, which implied that there was a better capacity comparatively. Furthermore, a comparative GCD test was performed at a constant current density of 2 A g^{-1} to study the charge–discharge behavior, as shown in Fig. 4(b). The asymmetric and non-linear GCD curves were demonstrated by all the BCS-x electrodes, which indicated the faradaic type of energy storage behavior occurring from the redox reactions at the electrode–electrolyte interface. The GCD curves demonstrated two distinguishable plateaus showing the two redox transitions of the electrons. These results exactly coincided with the obtained CV results. The BCS-1 electrode exhibited the superior discharge time among the BCS-x electrodes. Considering the integral area under discharge time, the C_{ts} values were calculated as 38, 290, and 57 mA h g^{-1} for the BCS-0.5, BCS-1, and BCS-2 electrodes, respectively, and these are shown as a bar graph in Fig. 4(c). Next, the CV test was performed for all the prepared BCS-x electrodes with a constant OPW (−1.2 to 0 V) at various scan rates ranging from 5 to 100 mV s^{-1}, as shown in Fig. 4(d), and Fig. S2(c and d) in the ESI.† A gradual increase in the current peak, together with no considerable variation in the curves of respective voltammo-

grams, was observed for all the prepared electrodes. This means that there is low equivalent series resistance and outstanding rate performance for all of the BCS-x electrodes.[27,28] A considerable shift in the redox peaks was observed towards the higher sites of the anodic and cathodic sides with an increase in the scan rate, probably due to the concentration polarization during the electrochemical activity.[29] The GCD assessment was performed at various current densities ranging from 2 to 15 A g^{-1} for all the BCS-x electrodes as shown in Fig. 4(e), and Fig. S2(e and f) in the ESI.† All the electrodes retained the GCD curves shape at high current densities, indicating excellent rate capability. Furthermore, the C_{ts} values for individual current densities were calculated from the discharge times of the GCD curves for all the BCS-x electrodes, and the comparative graph was plotted as shown in Fig. 4(f). Because of the integrity of the suitable nanosheet arrays, the BCS-1 electrode offered the highest C_{ts} at all the individual current densities among the BCS-x electrodes. The impressive C_{ts} of the BCS-1 is probably due to the synergistic effects of strong adhesion, interconnected nanosheet arrays, and optimal Bi/Cu molar concentration. Additionally, the TEM results demonstrated that the nanosheets with satisfactory transparency suggest that there is a thin 2D morphology. Low-dimensional nanostructures are an important candidate for surface/interface related applications such as SCs due to their interesting properties such as a high surface-to-volume ratio, low radius of curvature, high electron kinetics, and better thermal and chemical stabilities. According to a previous report, nanosheet-like surface morphology had a larger specific surface area (SSA) when compared to the nanorods- and particle-like structures.[15] In this respect, the thin nanosheet arrays of the BCS-1 provided enhanced accessible reaction sites and electrolyte diffusion, favoring the surface reactions, which lead to rapid ion/electron kinetics. The relatively low C_{ts} of the BCS-0.5 and BCS-2 can be explained by the respective FE-SEM and TEM images. The nanosheets infused with coagulated nanoparticle arrays of BCS-0.5 and increased thickness with shortening of length and non-uniformity of sheets of the BCS-2 hinder the electron transport, leading to the limitation of electron transfer.

By virtue of the electrochemical analysis, an increase in the current density leads to insufficient time for full utilization of the electroactive site by the electrolyte, and a gradual decrease in the C_{ts} was observed for all the electrodes at high current densities. From the electrochemical results, an excellent C_{ts} with a wide OPW (0 to −1.2 V) enabled the potential application of the BCS-1 electrode as a negative electrode for high-performance SC. To further investigate the total resistance offered by the electrochemical system for individual electrodes, EIS analysis was performed on individual electrodes. Comparative Nyquist plots of the BCS-x electrodes are shown in Fig. 4(g). All the electrodes demonstrated a straight line in the lower frequency region, which is related to the resistance offered by the diffusion limiting process (Warburg impedance). The EIS results were consistent with the obtained CV and GCD results. Among the BCS-x electrodes, the BCS-1 elec-
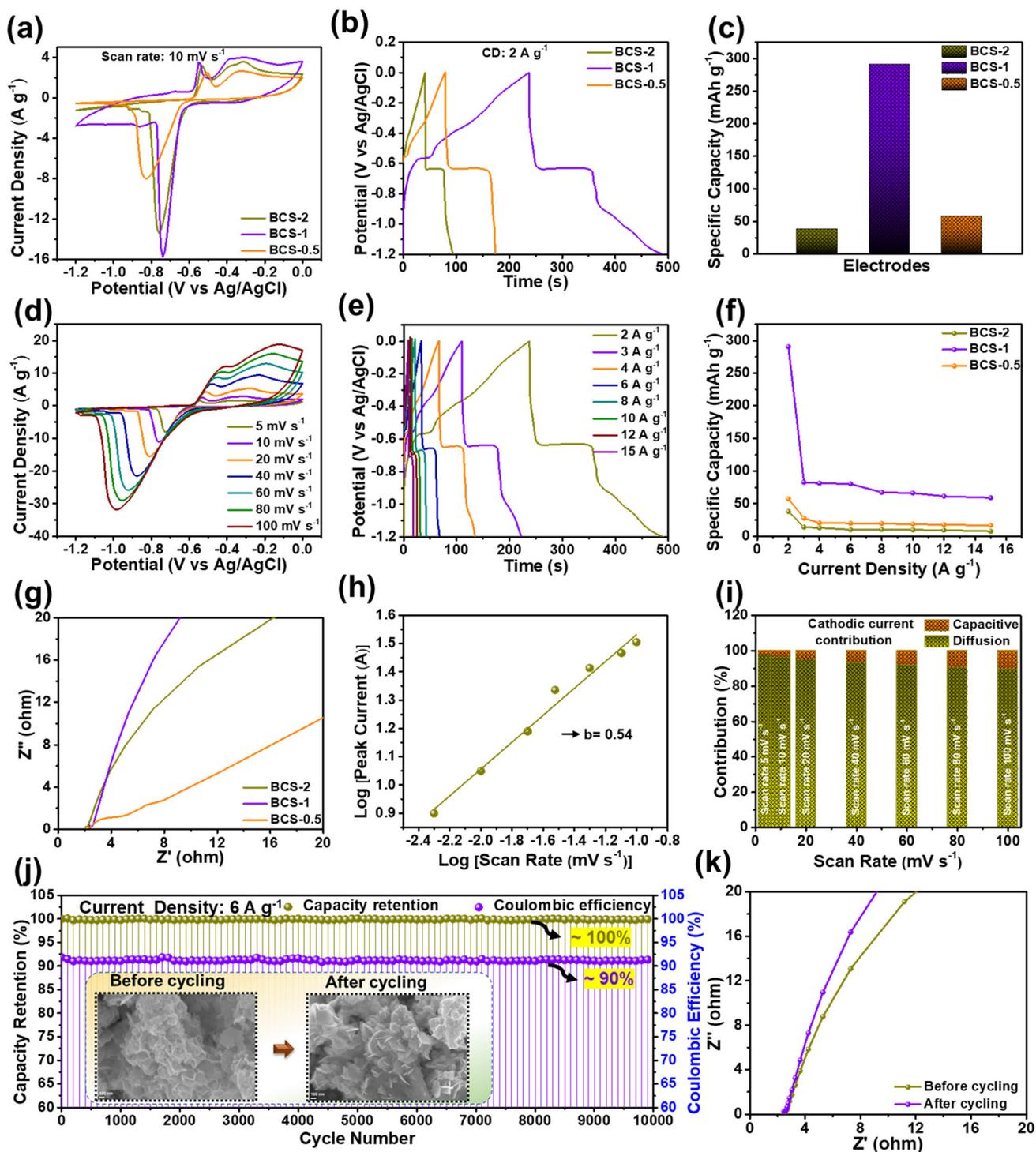
3276 | Inorg. Chem. Front., 2024, 11, 3270–3284

This journal is © the Partner Organisations 2024

Fig. 4 Comparisons of (a) CV curves, (b) GCD curves, and (c) C_{ts} values at 2 A g^{-1} of all the prepared BCS-*x* electrodes. (d) CV curves at different scan rates and (e) GCD curves at different current densities of the BCS-1 electrode. Comparisons of (f) C_{ts} values *vs*. current densities and (g) EIS plots of the BCS-*x* electrodes. (h) Relationship between the peak current density and scan rate to determine the *b* value and (i) total charge storage contribution at individual scan rates for the BCS-1. (j) Prolonged cycling stability test result and (k) EIS plots before and after the cycling measurement. The inset of (j) shows the FE-SEM images before and after the cycling test.

trode demonstrated a straight line inclined towards the *y*-axis. This implied that there was high electron transfer, ion diffusion, and electrical conductivity at the interface of the electrode and electrolyte, which is beneficial for enhancing the electrochemical properties. From the CV results, the BCS-1 electrode demonstrated redox peaks at all the scan rates,

This journal is © the Partner Organisations 2024

Inorg. Chem. Front., 2024, **11**, 3270–3284 | **3277**

which shows the excellent electrochemical reversibility and rapid charge transfer of the electrode. However, all the nano-structure-based electrodes store charge by both surface-controlled capacitive and diffusion-controlled processes. To further investigate the dominant energy storage by the BCS-1 electrode, a modified power law equation was employed:[29]

$$\log i = \log a + b \log v \qquad (4)$$

where i represents the current response and a and b are adjustable parameters. The b value is equal to the slope obtained from eqn (4). Typically, $b \sim 0.5$ and 1 represent the dominant diffusion-controlled and surface-controlled capacitive processes-based energy storage by the electrode, respectively.[30] The b value for the BCS-1 electrode was calculated using the cathodic CV peaks from 5 to 100 mV s^{-1}, and the value obtained was 0.54 which shows the dominant diffusion-controlled process-based charge storage behavior, as shown in Fig. 4(h). To further quantify the surface-controlled capacitive and diffusion-controlled charge storages by the BCS-1 electrode at individual scan rates, eqn (5) was used:

$$\frac{i}{v^{1/2}} = k_1 v^{1/2} + k_2 \qquad (5)$$

Here, k_1 and k_2 are the adjustable parameters. The relative current contribution ratio by the BCS-1 electrode at individual scan rates was estimated, and the bar graph obtained is shown in Fig. 4(i). The results coincide with the b value, indicating the dominance of the diffusion-based charge storage at all of the scan rates. For the commercialization of the electrode, cycling stability plays a crucial role. Continuous 10 000 GCD cycles were performed at a current density of 6 A g^{-1} for the BCS-1 electrode, as shown in Fig. 4(j). From the results, the BCS-1 electrode demonstrated excellent cycling stability with ~100% capacity retention and ~90% coulombic efficiency over 10 000 GCD cycles. In order to study the morphological stability of the electrode, the FE-SEM images were observed for the BCS-1 electrode before and after the cycling test, as shown in the inset of Fig. 4(j). After the cycling, the electrode retained almost the original morphology of the nanosheet arrays, suggesting that there was good morphological stability and strong adhesion of the electrode material with the CC, which exactly coincides with the cycling results. Furthermore, the EIS analysis of the electrode was performed before and after the cycling test, which demonstrated that the Nyquist plots were almost identical with a marginal shift of the straight line towards the y-axis in the lower frequency region after the cycling as shown in Fig. 4(k). This suggests that there was improved conductivity over the cycling period. The excellent cycling stability can be attributed to the interconnected vertically aligned nanosheet arrays and the strong material adhesion to the current collector, which benefits the fast electrolyte ion/electron transportation. Furthermore, the electrochemical performance of the BCS-1 electrode was compared with previous literature as summarized in Table 2.

Furthermore, a comparison of the XRD and Raman spectroscopy analyses for the BCS-1 electrode was performed

Table 2 Comparison of the electrochemical performances of the BCS-1 electrode with those found in previous reports

Sample name	Potential window (V)	Specific capacity (mA h g^{-1})	No. of cycles	Cycling stability (%)	Ref.
CuS@MnS	1.1	89.77	3000	95.9	34
CuS	1.1	45.73	3000	80	34
BGNS-1	0.65	237	100	75	26
Bi$_2$S$_3$/FGS	0.9	262	5000	75	35
Co-S-80	0.6	147	1000	86.5	36
MoS$_2$/Mn$_3$O$_4$	0.5	50	2000	76	37
CoNi$_2$S$_4$	0.55	247	10 000	82	38
BCS-1	**1.2**	**290**	**10 000**	**100**	**Present work**

before and after cycling. From Fig. S2(g) in the ESI,† the Raman spectrum of the BCS-1 electrode before cycling demonstrated prominent peaks at 1364 and 1584 cm^{-1} which originated from the substrate (CC), and in addition, two peaks were observed at 610 and 306 cm^{-1} corresponding to the metal–sulfur bond stretching.[31] Similarly, the Raman spectrum of the BCS-1 electrode after cycling exhibited peaks at the same positions as those before cycling without considerable peak shift, but with a prominent decrease in the peak intensity which may be due to the continuous charge–discharge cycles. Additionally, the a comparative XRD analysis was performed for the BCS-1 electrode sample before and after cycling, as shown in Fig. S2(h) in the ESI.† Both samples demonstrated a similar XRD pattern without any significant peak shift, but there was a slight decrease in the FWHM value for the sample after cycling, which may be due to the continuous 10 000 GCD cycles. The results obtained suggest the excellent cycling stability of the prepared BCS-1 electrode in the long-term test.

Motivated by the excellent electrochemical performance of the BCS-1 electrode, the ASSSC device was fabricated using the electrode as a negative electrode, and a Ni element-based NS electrode was employed as a positive electrode. Prior to the device fabrication, the electrochemical properties of the NS electrode were determined. The CV curves were measured at various scan rates ranging from 5 to 10 mV s^{-1} with an OPW of 0 to 0.65 V as shown in Fig. 5(a). A significant increase in the current peak was observed with the increasing the scan rate, implying that there was an excellent rate capability. However, the shift of both anodic and cathodic peaks was observed upon the increase in scan rate, which typically corresponds to the concentration polarization at the interface of the electrode and electrolyte.[32] The GCD analysis was performed with a sequence of OPWs between 0 to 0.6 V at various current densities (2–15 A g^{-1}), and non-linear triangular symmetric GCD curves were observed at all the current densities, as shown in Fig. 5(b). This implies that the NS electrode has faradaic type of capacitive behavior. In Fig. 5(c), the C_{ts} value with respect to current density was calculated from the GCD analysis, demonstrating the maximum C_{ts} value of 178 mA h g^{-1} at 2 A g^{-1}. Fig. 5(d) shows the EIS plot of the NS electrode. A linear straight line at a lower frequency was observed, indicating

3278 | *Inorg. Chem. Front.*, 2024, **11**, 3270–3284
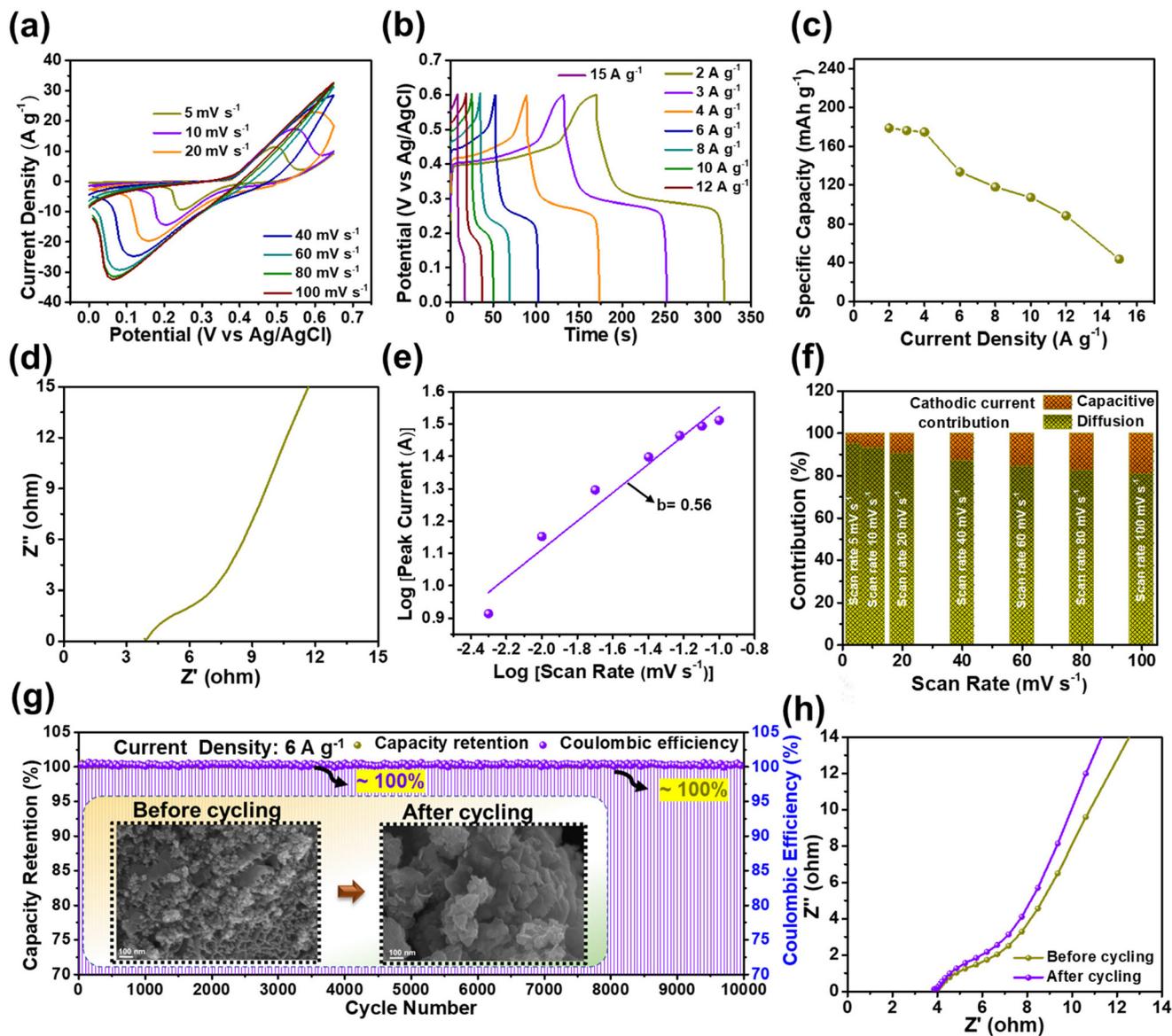
This journal is © the Partner Organisations 2024

Fig. 5 (a) CV curves at different scan rates, (b) GCD curves at different current densities, (c) C_{ts} values *vs.* current densities, and (d) EIS plots for the NS electrode. (e) Relationship between the peak current density and scan rate to determine the *b* value and (f) total charge storage contribution at individual scan rates for the NS electrode. (g) Prolonged cycling stability test and (h) EIS plots before and after the cycling test for the NS electrode. The inset of (g) shows the FE-SEM images of the NS electrode before and after the cycling test.

high ion diffusion, electron transfer, and electrical conductivity of the electrode, which improved the electrochemical properties. Fig. 5(e) shows the relationship between the peak current density and scan rate to determine the *b* value. To evidence the faradaic type of the charge storage mechanism of the NS electrode, the *b* value was calculated using eqn (4) from the cathodic peaks, and the value obtained was 0.56. Furthermore, the ratio of diffusion-controlled and surface-controlled charge storages was calculated using eqn (5) and these are shown in the bar graph of individual scan rates (Fig. 5(f)). From the results, a superior diffusion-controlled charge storage mechanism was observed at all the scan rates, suggesting that the dominant faradaic type charge storage was

by the NS electrode. Furthermore, the long-term cycling stability of the NS electrode was also determined, as shown in Fig. 5(g). As expected from the beneficial nanoparticle array morphology, the NS electrode demonstrated outstanding cycling stability with ~100% capacity retention and ~100% coulombic efficiency over 10 000 GCD cycles. Consequently, the morphological stability of the electrode was determined using the FE-SEM images of the sample before and after cycling, as shown in the inset of Fig. 5(g). After the cycling, the NS electrode retained almost the initial morphology of the nanoparticle arrays, which indicates excellent morphological stability and strong adhesion of the electrode material, which exactly overlapped with the cycling results. In addition, the EIS
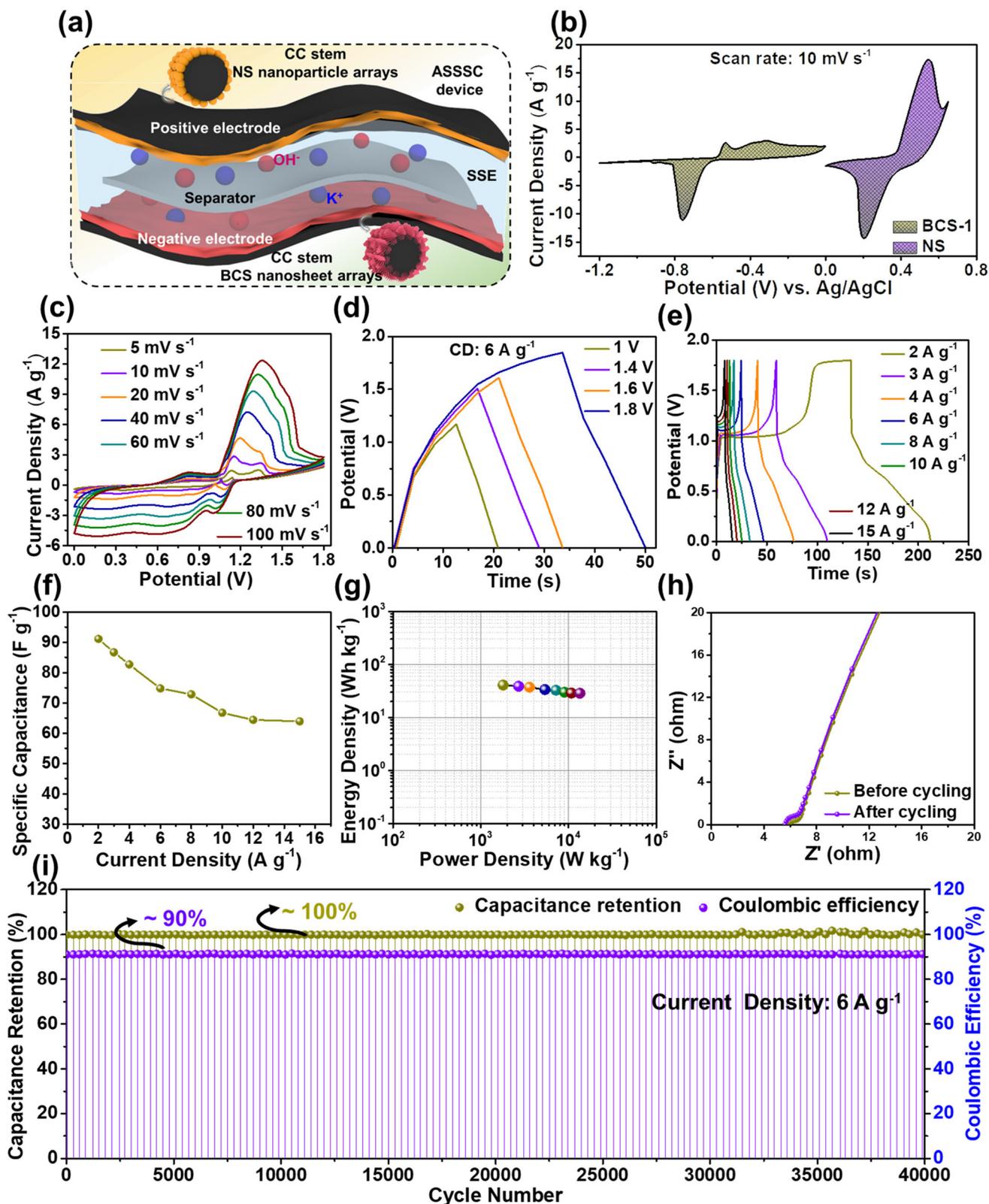
This journal is © the Partner Organisations 2024

Inorg. Chem. Front., 2024, **11**, 3270–3284 | **3279**

Fig. 6 (a) A schematic illustration of the as-assembled ASSSC device. (b) Merged CV plots of the NS and BCS-1 electrodes measured in a three-electrode system, (c) CV curves at different scan rates with the optimized OPW, (d) GCD curves at different potentials for optimization, and (e) GCD curves at different current densities with the optimized OPW for the ASSSC device. (f) C_s values *vs*. various current densities, (g) Ragone plot, (h) EIS plots before and after the cycling test, and (i) cycling stability performance for the ASSSC device.

3280 | *Inorg. Chem. Front.*, 2024, **11**, 3270–3284

This journal is © the Partner Organisations 2024

analysis of the NS electrode was performed before and after the cycling test, and identical Nyquist plots with a minimal shift of the straight line towards the *y*-axis in the lower frequency were observed after the cycling, as shown in Fig. 5(h), suggesting that there was enhanced conductivity over the cycling and supporting the cycling stability.

Fig. 6(a) shows the schematic representation of the electrolyte ion diffusion over the electrodes making up the ASSSC device during electrochemical analysis. The electrochemical properties of the ASSSC device were evaluated. To check the OPW of the fabricated ASSSC device, the CV curves of BCS-1 (−1.2 to 0 V) and NS (0 to 0.65 V) electrodes in a three-electrode system at a scan rate of 10 mV s^{-1} were plotted together, as shown in Fig. 6(b). This result suggests 0 to 1.8 V as an optimum OPW for the ASSSC device. Furthermore, the charge storage performance of the ASSSC device was initially investigated using CV analysis performed at various scan rates ranging from 5 to 100 mV s^{-1} with a fixed OPW (0 to 1.8 V) as shown in Fig. 6(c). The CV curves obtained at all the scan rates were composed of redox current peaks, indicating the faradaic type charge storage behavior of the ASSSC device, and a gradual increase in current response and no change in the shape of CV curve was observed upon increasing the scan rate, showing that the good rate performance resulted from beneficial ion/electron transport kinetics in the constituents of the electrodes of the ASSSC device. In addition, the GCD analysis was employed to investigate the charge–discharge performance of the ASSSC device. Previously, an optimum OPW was determined by performing the GCD analysis at various OPWs (1 to 1.8 V) with a fixed current density of 6 A g^{-1} (Fig. 6(d)). This result indicated that the optimum OPW of 0 to 1.8 V exactly coincided with the CV result. Furthermore, the GCD analysis was also recorded for the ASSSC device at various current densities (2 to 15 A g^{-1}) at the optimized OPW as shown in Fig. 6(e). The non-linear GCD curves indicate the faradaic type charge storage behavior by the ASSSC device, which is coincident with the CV result. Considering the discharge time, the C_s value was calculated at an individual current density as shown in Fig. 6(f). The ASSSC device delivered the maximum C_s value of 91 F g^{-1} at 2 A g^{-1} and retained 69% of the initial C_s value even at a high current density of 15 A g^{-1}, which indicates the good rate performance of the ASSSC device. From the electrochemical results, the energy and power density values were calculated for the ASSSC device, as illustrated in the Ragone plot (Fig. 6(g)). The ASSSC device successfully demonstrated the maximum power and energy density values of 13 500 W kg^{-1} and 41 W h kg^{-1}, respectively, which results from the synergetic effect of the constituents of the electrode of the ASSSC device. For practical applications, long-term cycling stability plays a crucial role. To verify this, a continuous 40 000 GCD cycling test was performed for the ASSSC device at a current density of 6 A g^{-1}. Typically, the SCs exhibit a dip in the capacity value during the initial GCD cycles due to the formation of substances containing OH^{-} causing changes in the morphological structures.[33] However, the ASSSC device demonstrated a negligible dip during the initial GCD cycles,

which shows the excellent morphological stability of the constituent electrodes and the overall maintenance of the ∼100% capacitance retention and ∼90% coulombic efficiency across the 40 000 GCD cycles, as shown in Fig. 6(i). Moreover, the EIS analysis was performed using the ASSSC device before and after the cycling test, which implied there was no distinct degradation (Fig. 6(h)). However, the straight line in the lower frequency shifted slightly towards the *y*-axis, indicating the excellent conductivity over the cycling. In addition, a comparative cycling stability test was performed at a low current density (2 A g^{-1}) and a high current density (6 A g^{-1}) for the ASSSC device by performing 20 000 continuous GCD cycles. The ASSSC device demonstrated almost overlapping cycling stability performance with a capacitance retention of ∼100% at both low and high current densities over 20 000 GCD cycles, showing the good long-term cycling stability of the ASSSC device at both low and high current densities, as shown in Fig. S3 of the ESI.† Finally, the electrochemical performance of the ASSSC device was compared with previously published reports, as summarized in Table 3.

With the developments in advanced portable electronics, flexible SCs are becoming more desirable in energy storage systems, which are anticipated to operate under a mechanically contorted state. Next, to determine the flexibility effect on the electrochemical properties, the CV measurements were performed for the ASSSC device under various mechanically contorted states (ideal, twisting, bending, and finger movement modes). The obtained CV curves were almost identical to each other, validating the mechanical stability of the ASSSC device without sacrificing any capacitive performance. To further verify the performance and practical application under a contorted state, serially connected two ASSSC devices were attached to human fingers and further employed to power the liquid crystal display (LCD), and the electrical fan with various finger movements (single finger movement and double finger movement) and these were compared with the ideal state. As expected from an excellent electrochemical performance by the ASSSC device, serially connected devices successfully powered the LCD and electrical fan under all the finger movements without any power loss, as shown in Fig. 7. The results

Table 3 Comparison of the electrochemical performances of the ASSSC device with those in previous reports

Device name	Potential window (V)	ED (W h kg^{-1})	No. of cycles	Cycling stability (%)	Ref.
BMP-2//AC	1.8	31.9	6000	86.5	39
CuS@CD-GOH	1.4	28	5000	90	40
Bi$_2$O$_3$@MnO$_2$// Bi$_2$O$_3$@MnO$_2$	1.2	28	2000	72	41
TCBOC//TCBOC	1.2	15.2	5000	85	42
(Fe(III)/BiOCl)// (Fe(III)/BiOCl)	1	17	5000	72	43
BM//AC	1.2	14.4	5000	90	44
H-CuS//AC	1.6	15.97	20 000	89	9
ASSSC	**1.8**	**41**	**40 000**	**100**	**Present work**

This journal is © the Partner Organisations 2024

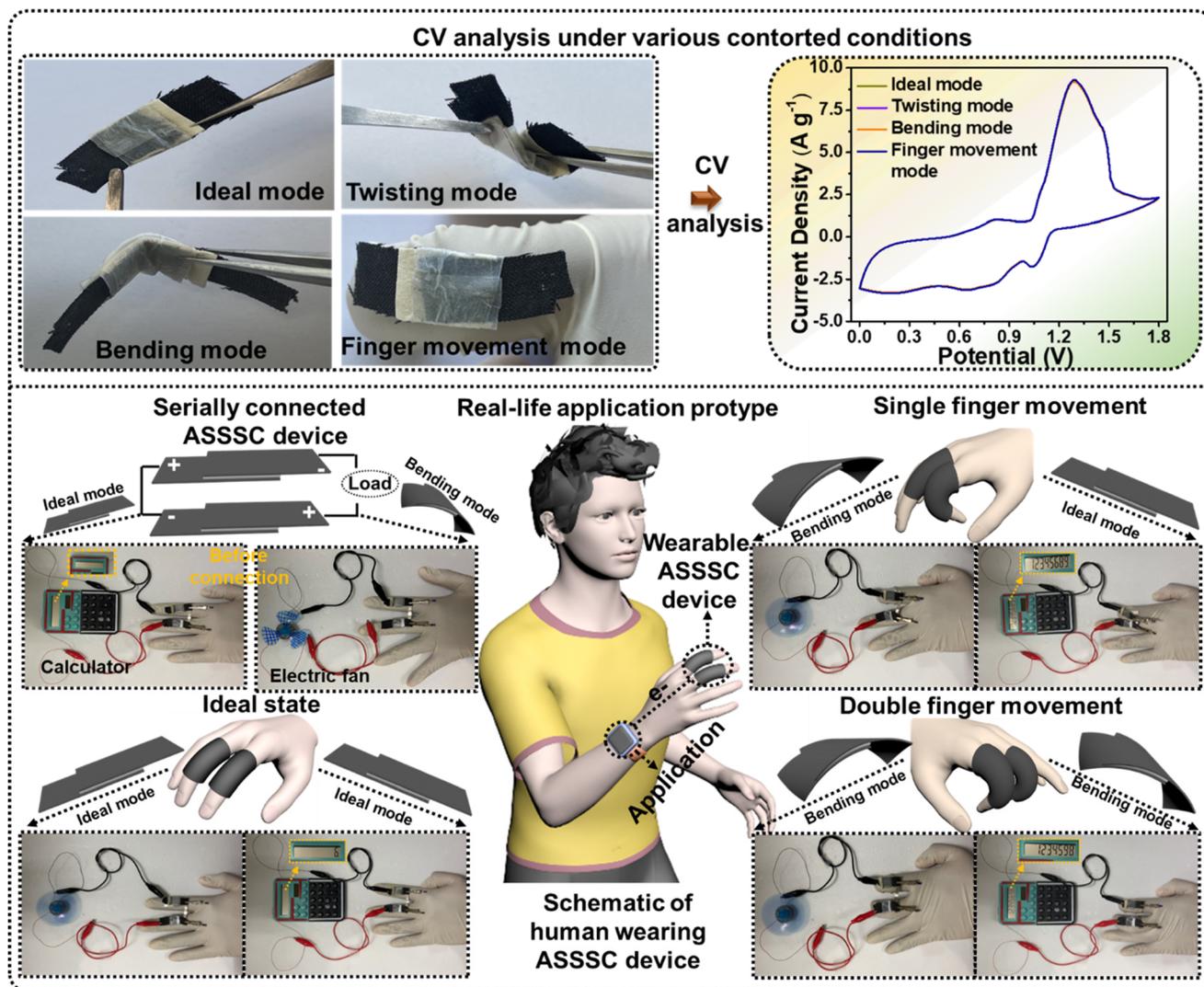*Inorg. Chem. Front.*, 2024, **11**, 3270–3284 | **3281**

Fig. 7 CV analysis of the ASSSC device under various contorted conditions. Real-time practical application of two serially connected ASSSC devices attached to human fingers, demonstrating their wearability and powering of an LCD and an electrical fan with single finger movement and double finger movement in comparison with the ideal state.

indicate the excellent flexibility and mechanical stability of the ASSSC device, suggesting the potential application of a wide OPW ASSSC device with high power and energy densities for flexible energy storage systems.

4. Conclusions

The present study demonstrated the synthesis of flexible BCS *via* the ED method for use as a negative electrode. The effect of the molar concentration ratio of Bi and Cu in the growth solution on the crystal structure and surface morphology was also investigated as $Bi_xCu_{3-x}S_3$. The optimum surface morphology of the nanosheet arrays was obtained with "$x = 1$" in the growth solution of $Bi_xCu_{3-x}S_3$. The BCS-1 electrode revealed excellent electrochemical properties with a C_{ts} value of 290 mA

h g^{-1}. The BCS-1 electrode material with a vertically aligned interconnected 3D network of nanosheet arrays provided continuous channels for rapid electron/ion transfer and firm adhesion with CC, eventually exhibiting an excellent cycling stability of ~100% capacity retention across 10 000 GCD cycles to the initial cycle. Furthermore, a novel all-sulfide gel electrolyte-based ASSSC device was fabricated using the BCS-1 and NS as the negative and positive electrodes, respectively. The ASSSC device delivered the maximum power and energy density values of 13 500 W kg^{-1} and 41 W h kg^{-1}, respectively and overall maintained ~100% capacity retention across the 40 000 GCD cycles. To validate the application of the ASSSC device under contorted conditions, two serially connected ASSSC devices were attached to human fingers and further employed to power the LCD and electrical fan with various finger movements. As a result, the ASSSC device successfully powered

3282 | *Inorg. Chem. Front.*, 2024, **11**, 3270–3284

This journal is © the Partner Organisations 2024

them without any power loss, verifying the application of the ASSSC device as a wearable energy storage device. The prototype of the ASSSC device is cost-effective, scalable, and simple, showing the synthesis of novel all-sulfide flexible electrodes for advanced flexible, portable, and wearable electronic applications.

Conflicts of interest

There are no conflicts to declare.

Acknowledgements

References

1 A. Vlad, N. Singh, J. Rolland, S. Melinte, P. M. Ajayan and J. F. Gohy, Hybrid supercapacitor-battery materials for fast electrochemical charge storage, *Sci. Rep.*, 2014, **4**, 1–7.

2 X. Liu, W. Xu, D. Zheng, Z. Li, Y. Zeng and X. Lu, Carbon cloth as an advanced electrode material for supercapacitors: progress and challenges, *J. Mater. Chem. A*, 2020, **8**, 17938–17950.

3 G. Xiong, P. He, B. Huang, T. Chen, Z. Bo and T. S. Fisher, Graphene nanopetal wire supercapacitors with high energy density and thermal durability, *Nano Energy*, 2017, **38**, 127–136.

4 N. S. Shaikh, S. B. Ubale, V. J. Mane, J. S. Shaikh, V. C. Lokhande, S. Praserthdam, C. D. Lokhande and P. Kanjanaboos, Novel electrodes for supercapacitor: Conducting polymers, metal oxides, chalcogenides, carbides, nitrides, MXenes, and their composites with graphene, *J. Alloys Compd.*, 2022, **893**, 161998.

5 N. Hillier, S. Yong and S. Beeby, The good, the bad and the porous: A review of carbonaceous materials for flexible supercapacitor applications, *Energy Rep.*, 2020, **6**, 148–156.

6 K. K. Upadhyay, T. Nguyen, T. M. Silva, M. J. Carmezim and M. F. Montemor, Electrodeposited MoO_x films as negative electrode materials for redox supercapacitors, *Electrochim. Acta*, 2017, **225**, 19–28.

7 R. Sahoo, D. T. Pham, T. H. Lee, T. H. T. Luu, J. Seok and Y. H. Lee, Redox-Driven Route for Widening Voltage Window in Asymmetric Supercapacitor, *ACS Nano*, 2018, **12**, 8494–8505.

8 M. Xu, Y. Niu, X. Teng, S. Gong, L. Ji and Z. Chen, High-capacity Bi_2O_3 anode for 2.4 V neutral aqueous sodium-ion battery-supercapacitor hybrid device through phase conversion mechanism, *J. Energy Chem.*, 2022, **65**, 605–615.

9 Y. Liu, Z. Zhou, S. Zhang, W. Luo and G. Zhang, Controllable synthesis of CuS hollow microflowers hier-

archical structures for asymmetric supercapacitors, *Appl. Surf. Sci.*, 2018, **442**, 711–719.

10 Z. Pan, F. Cao, X. Hu and X. Ji, A facile method for synthesizing CuS decorated Ti_3C_2 MXene with enhanced performance for asymmetric supercapacitors, *J. Mater. Chem. A*, 2019, **7**, 8984–8992.

11 S. Ghosh, P. Samanta, N. C. Murmu and T. Kuila, Investigation of electrochemical charge storage in nickel-cobalt-selenide/reduced graphene oxide composite electrode and its hybrid supercapacitor device, *J. Alloys Compd.*, 2020, **835**, 155432.

12 B. Qin, X. Zhao, Q. Wang, W. Yao, Y. Cai, Y. Chen, P. Wang, Y. C. Zou, J. Cao, X. Zheng, J. Qi and W. Cai, A tandem electrocatalyst with dense heterointerfaces enabling the stepwise conversion of polysulfide in lithium-sulfur batteries, *Energy Storage Mater.*, 2023, **55**, 445–454.

13 F. Qi, L. Shao, X. Shi, F. Wu, H. Huang, Z. Sun and A. Trukhanov, "Carbon quantum dots-glue" enabled high-capacitance and highly stable nickel sulphide nanosheet electrode for supercapacitors, *J. Colloid Interface Sci.*, 2021, **601**, 669–677.

14 Y. Yan, J. Lin, K. Huang, X. Zheng, L. Qiao, S. Liu, J. Cao, S. C. Jun, Y. Yamauchi and J. Qi, Tensile Strain-Mediated Spinel Ferrites Enable Superior Oxygen Evolution Activity, *J. Am. Chem. Soc.*, 2023, **145**, 24218–24229.

15 E. G. Shankar, A. K. Das and J. S. Yu, Facile one-step electrodeposition synthesis of binder-free $Co_xFe_{3(-x)}Se_4$ ultrathin nanosheet arrays towards high-performance quasi-solid-state supercapacitors, *Appl. Surf. Sci.*, 2022, **596**, 153613.

16 E. G. Shankar, A. K. Das and J. S. Yu, Biomass-derived ant colony-like ion diffused redox porous carbon toward economical and high-performance quasi-solid-state supercapacitor, *Int. J. Energy Res.*, 2022, **46**, 1593–1608.

17 A. K. Das, E. G. Shankar, B. Ramulu and J. S. Yu, Electrochemical performance of asymmetric supercapacitor with binder-free $Co_xMn_{3(-x)}Se_4$ and radish-derived carbon electrodes using $K_3[Fe(CN)_6]$ additive in electrolyte, *Chem. Eng. J.*, 2022, **448**, 137725.

18 E. G. Shankar, A. K. Das and J. S. Yu, Entire onion source-derived redox porous carbon electrodes towards efficient quasi-solid-state solar charged hybrid supercapacitor, *J. Mater. Sci. Technol.*, 2022, **125**, 118–127.

19 E. G. Shankar, M. Aishwarya, A. Khan, A. B. V. K. Kumar and J. S. Yu, Efficient solar light photocatalytic degradation of commercial pharmaceutical drug and dye using rGO-PANI assisted c-ZnO heterojunction nanocomposites, *Ceram. Int.*, 2021, **47**, 23770–23780.

20 D. A. Zatsepin, A. F. Zatsepin, D. W. Boukhvalov and N. V. Gavrilov, Bi-doped silica glass: A combined XPS – DFT study of electronic structure and pleomorphic imperfections, *J. Alloys Compd.*, 2020, **829**, 154459.

21 N. K. Gupta, S. Kim, J. Bae and K. S. Kim, Chemisorption of hydrogen sulfide over copper-based metal-organic frameworks: Methanol and UV-assisted regeneration, *RSC Adv.*, 2021, **11**, 4890–4900.

This journal is © the Partner Organisations 2024

Inorg. Chem. Front., 2024, **11**, 3270–3284 | **3283**

22 S. Adhikari, D. Sarkar and G. Madras, Hierarchical Design of CuS Architectures for Visible Light Photocatalysis of 4-Chlorophenol, *ACS Omega*, 2017, **2**, 4009–4021.

23 Z. Jin, C. Liu, K. Qi and X. Cui, Photo-reduced Cu/CuO nanoclusters on TiO$_2$ nanotube arrays as highly efficient and reusable catalyst, *Sci. Rep.*, 2017, **7**, 1–9.

24 B. Ye, X. Cao, Q. Zhao, A. Zhou and J. Wang, Free-standing NiCoSe$_2$ nanostructure on Ni foam via electrodeposition as high-performance asymmetric supercapacitor electrode, *Nanotechnology*, 2020, **31**, 335706.

25 G. Zhang, H. Xuan, J. Yang, R. Wang, Z. Xie, X. Liang, P. Han and Y. Wu, Preparation and characterization of novel 2D/3D NiSe$_2$/MnSe grown on rGO/Ni foam for high-performance battery-supercapacitor hybrid devices, *J. Power Sources*, 2021, **506**, 230255.

26 G. Nie, X. Lu, J. Lei, L. Yang and C. Wang, Facile and controlled synthesis of bismuth sulfide nanorods-reduced graphene oxide composites with enhanced supercapacitor performance, *Electrochim. Acta*, 2015, **154**, 24–30.

27 S. Zheng, Y. Fu, L. Zheng, Z. Zhu, J. Chen, Z. Niu and D. Yang, PEDOT-engineered Bi$_2$O$_3$ nanosheet arrays for flexible asymmetric supercapacitors with boosted energy density, *J. Mater. Chem. A*, 2019, **7**, 5530–5538.

28 A. K. Das, B. Ramulu, E. G. Shankar and J. S. Yu, Binder-free CuS@PEDOT and Co–V–Se electrodes for flexible quasi-solid-state asymmetric supercapacitor, *Chem. Eng. J.*, 2022, **429**, 132486.

29 A. K. Das, U. N. Pan, V. Sharma, N. H. Kim and J. H. Lee, Nanostructured CeO$_2$/NiV–LDH composite for energy storage in asymmetric supercapacitor and as methanol oxidation electrocatalyst, *Chem. Eng. J.*, 2021, **417**, 128019.

30 A. Ajay, A. Paravannoor, J. Joseph, V. Amruthalakshmi, S. S. Anoop, S. V. Nair and A. Balakrishnan, 2 D amorphous frameworks of NiMoO$_4$ for supercapacitors: Defining the role of surface and bulk controlled diffusion processes, *Appl. Surf. Sci.*, 2015, **326**, 39–47.

31 O. Rabin, J. M. Perez, J. Grimm, G. Wojtkiewicz and R. Weissleder, An X-ray computed tomography imaging agent based on long-circulating bismuth sulphide nanoparticles, *Nat. Mater.*, 2006, **5**, 118–122.

32 V. Tezyk, C. Rossignol, N. Sergent, E. Djurado, J. Laurencin and E. Siebert, Cyclic voltammetry and high-frequency series resistance of La$_{0.6}$Sr$_{0.4}$Co$_{0.2}$Fe$_{0.8}$O$_{3-\delta}$ electrode deposited on GDC: Effect of the electrode microstructure and the oxygen partial pressure, *Electrochim. Acta*, 2019, **304**, 312–322.

33 Q. Fang, M. Sun, X. Ren, Y. Sun, Y. Yan, Z. Gan, J. Huang, B. Cao, W. Shen, Z. Li and Y. Q. Fu, Hydrothermal synthesis of cobalt sulfide nanotubes: The size control and its appli-cation in supercapacitors, *J. Colloid Interface Sci.*, 2022, **611**, 503–512.

34 P. Himasree, I. K. Durga, T. N. V. Krishna, S. S. Rao, C. V. V. Muralee Gopi, S. Revathi, K. Prabakar and H. J. Kim, One-step hydrothermal synthesis of CuS@MnS on Ni foam for high performance supercapacitor electrode material, *Electrochim. Acta*, 2019, **305**, 467–473.

35 H. Lu, Q. Guo, F. Zan and H. Xia, Bi$_2$S$_3$ nanoparticles anchored on graphene nanosheets with superior electrochemical performance for supercapacitors, *Mater. Res. Bull.*, 2017, **96**, 471–477.

36 H. Wan, X. Ji, J. Jiang, J. Yu, L. Miao, L. Zhang, S. Bie, H. Chen and Y. Ruan, Hydrothermal synthesis of cobalt sulfide nanotubes: The size control and its application in supercapacitors, *J. Power Sources*, 2013, **243**, 396–402.

37 M. Wang, H. Fei, P. Zhang and L. Yin, Hierarchically Layered MoS$_2$/Mn$_3$O$_4$ Hybrid Architectures for Electrochemical Supercapacitors with Enhanced Performance, *Electrochim. Acta*, 2016, **209**, 389–398.

38 S. Rafai, C. Qiao, M. Naveed, Z. Wang, W. Younas, S. Khalid and C. Cao, Microwave-anion-exchange route to ultrathin cobalt-nickel-sulfide nanosheets for hybrid supercapacitors, *Chem. Eng. J.*, 2019, **362**, 576–587.

39 F. Wu, X. Wang, W. Zheng, H. Gao, C. Hao and C. Ge, Synthesis and characterization of hierarchical Bi$_2$MoO$_6$/Polyaniline nanocomposite for all-solid-state asymmetric supercapacitor, *Electrochim. Acta*, 2017, **245**, 685–695.

40 B. De, T. Kuila, N. H. Kim and J. H. Lee, Carbon dot stabilized copper sulphide nanoparticles decorated graphene oxide hydrogel for high performance asymmetric supercapacitor, *Carbon*, 2017, **122**, 247–257.

41 Z. A. Shaikh, P. V. Shinde, S. F. Shaikh, A. M. Al-Enizi and R. S. Mane, Facile synthesis of Bi$_2$O$_3$@MnO$_2$ nanocomposite material: A promising electrode for high performance supercapacitors, *Solid State Sci.*, 2020, **102**, 106158.

42 Q. X. Xia, N. M. Shinde, J. M. Yun, T. Zhang, R. S. Mane, S. Mathur and K. H. Kim, Bismuth Oxychloride/MXene symmetric supercapacitor with high volumetric energy density, *Electrochim. Acta*, 2018, **271**, 351–360.

43 R. Rameshbabu, M. Sandhiya and M. Sathish, Fe(III) ions grafted bismuth oxychloride nanosheets for enhanced electrochemical supercapacitor application, *J. Electroanal. Chem.*, 2020, **862**, 113958.

44 A. M. Teli, T. S. Bhat, S. A. Beknalkar, S. M. Mane, L. S. Chaudhary, D. S. Patil, S. A. Pawar, H. Efstathiadis and J. Cheol Shin, Bismuth manganese oxide based electrodes for asymmetric coin cell supercapacitor, *Chem. Eng. J.*, 2022, **430**, 133138.

3284 | *Inorg. Chem. Front.*, 2024, **11**, 3270–3284

This journal is © the Partner Organisations 2024